Faculté des Sciences Appliquées

BEMT Project
Analysis of a NACA propeller

AERO0014 – Aerospace propulsion

Authors: Victor Renkin

ID : s2306326

Instructor:	Koen Hillewaert
Teaching Assistant:	Maxime Borbouse
Academic year :	2023-2024

26th August 2024

Contents

1 Introduction

The objective of this study is to replicate the experimental findings reported by Biermann et al. [1] using the test setup illustrated in Figure 1.1, employing the Blade Element Momentum Theory (BEMT). This investigation further extends to analyzing the design and control mechanisms of the propellers tested. The propellers under scrutiny were uniformly three-bladed, each with a diameter of 10 feet, powered by a Curtiss Conqueror engine (GIV-1570). The subsequent sections will primarily focus on the propeller modeled with the Clark Y blade profile, referred to as 5868-9.

1.1 Propeller Specification

The blade geometry is defined by a figure in [1]. The objective is to replicate Figure 1.1a from [1] to capture identical data, thereby facilitating a comparison with other results referenced in the same publication. Data is extracted from Figure Figure 1.1a and subjected to polynomial approximation. An extrapolation is performed to estimate the value of p at $r/R = 1$. Additionally, b is assumed to be 0 at $r/R = 1$. The number of elements for this study is set to 100 elements per blade. This number was determined by examining the convergence discussed in Appendix A. This approach allows for an optimal balance between compile time and precision.

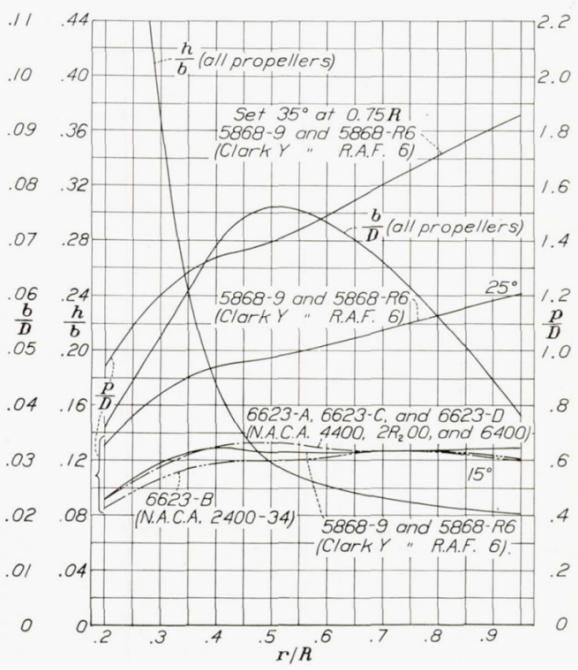

(a) Blade form curves [1]

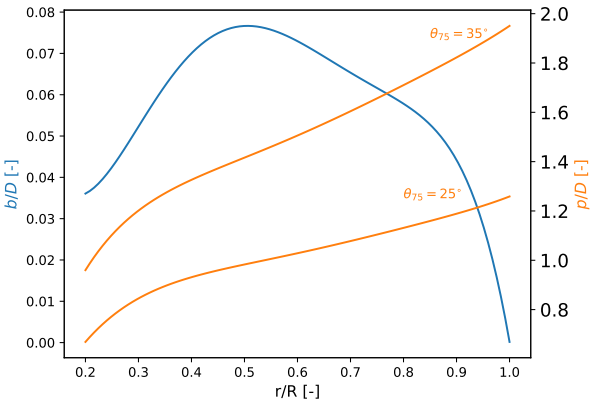

(b) Reproduction of the blade curve from [1] using a polynomial approximation

Figure 1.1: Comparative blade form curves.

2 Comparison of the Polynomial Law for Blade Section Polars with Clark Polar Data

The objective of this section is to compare the polynomial laws for the polars of the blade sections with the Clark polar data. The polynomial laws are defined as follows:

$$c_l(\alpha) = 0.1101 \times \alpha + 0.4409, \qquad c_d(\alpha) = 0.0006 \times \alpha^2 - 0.0042 \times \alpha + 0.0050, \quad (1)$$

where α represents the angle of attack in degrees. These polynomial laws are compared with the actual Clark polar data obtained from MATLAB using the function clarkypolarsRe(aoa, re) [2]. It is important to note that the clarkypolarsRe function requires the input of the Reynolds number. Consequently, the Reynolds number must be considered when interpreting the data. Figure 2.1 presents the Reynolds number in relation to the angle of attack.

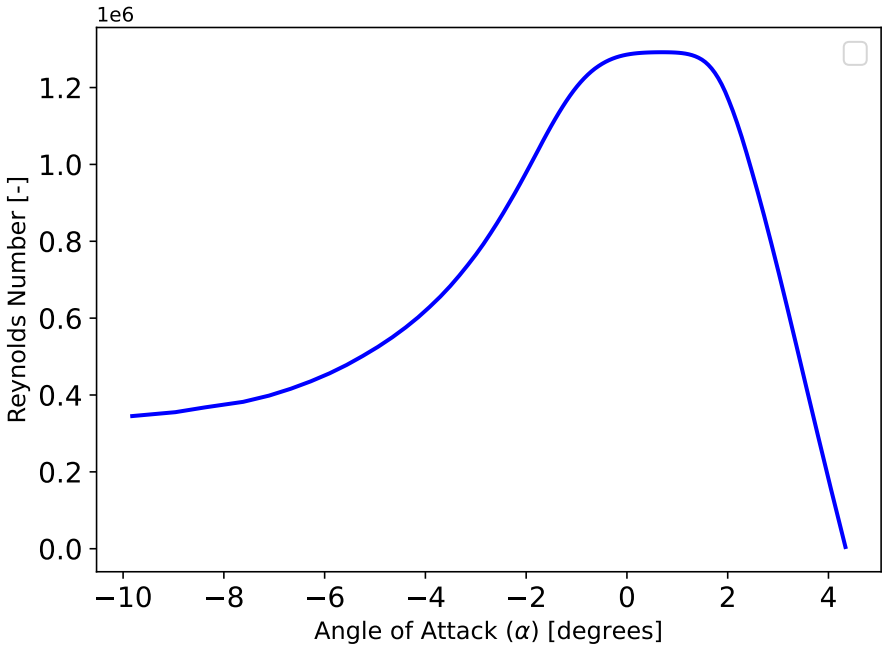

Figure 2.1: The number of Reynold in function of the angle of attack.

2.1 Lift Comparison

At high angles of attack, some perturbations are noticeable like discernible, as illustrated in Figure 2.2. However, they are not substantial. The lift is not greatly influenced by the Reynolds number; instead, an earlier stall occurs if the Reynolds number is low, as observed towards the end of the graph, where we have a high angle of attack and so can have some stall.

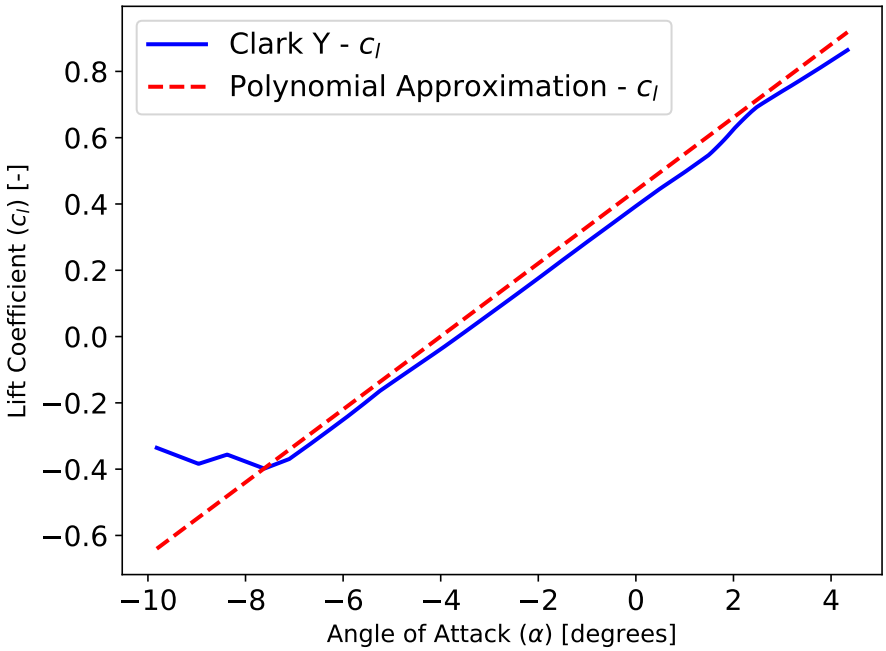

Figure 2.2: Comparison of Lift Coefficients vs. angle of attack.

2.2 Drag comparaison

The same pattern is observed for drag, as show in Figure 2.3. However, the impact is more pronounced. Drag is significantly affected by separation, leading to an increase in pressure drag and, consequently, a substantial rise in overall drag. By examining the drag, a clearer understanding of the Reynolds number's effect on stall can be achieved. A higher Reynolds number results in a turbulent boundary layer, which is more resistant to separation, delaying the onset of separation and thus reducing drag. Before separation occurs, the Reynolds number has a minimal effect on drag, which explains the relative stability observed before -5°.

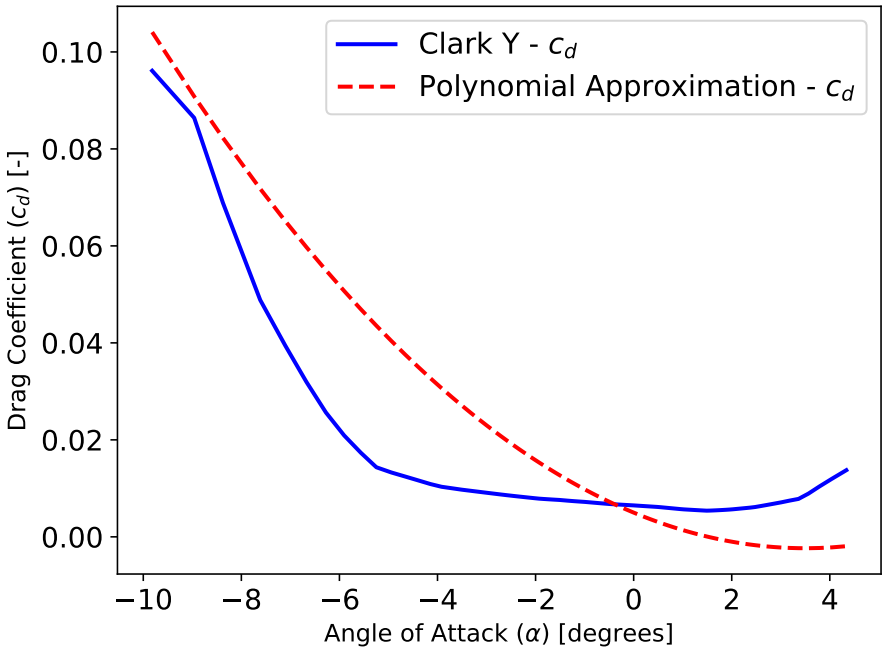

Figure 2.3: Comparison of Drag Coefficients vs. α.

In conclusion, before stall both lift and drag can be approximated by polynomial functions as the Reynolds number does not have a significant effect in this region. However, after stall, there is a more pronounced increase in drag compared to lift, which is why lift can be approximated by taking all points and the points of separation will not have much effect compared to drag which will have a much greater effect. That's why it's important to know when the separation occurs in order to use such an approximation.

3 Thrust and Power Distribution along the Span

In this section, the discussion is limited to a rotational speed of 800 RPM. The goal of this section is to understand the trust and power distribution along the span with two different configuration at their designed point, which is defined as the selected wind speed corresponds to a point with maximum propulsion efficiency as depicted in Figure 4.3 within subsection 4.3. The two configuration are the pitch angle at three-quarter span $\theta_{75} = 25°$ at a wind speed of 90 mph, and for $\theta_{75} = 35°$ at a wind speed of 135 mph. The results of the thrust, power absorbed by the propeller and propulsive efficiency are depicted in Table 3.1 for both configurations.

	$\theta_{75} = 25°,\ v_\infty = 90$ mph	$\theta_{75} = 35°,\ v_\infty = 135$ mph
Thrust T [N]	1223.3	1479.6
Power absorbed by the propeller P [kW]	54.4	96.5
Propulsive efficiency η [-]	0.904	0.925

Table 3.1: Propeller results at two different configurations, as rotational speed is 800 RPM.

To analyze Figure 3.1, the process will be divided into two steps: first, analyzing the curve; second, examining the differences between the two configurations.

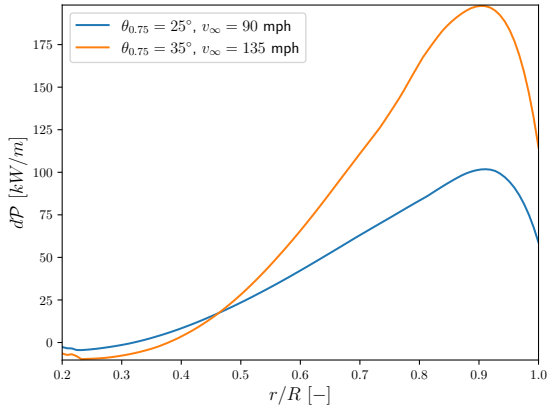

(a) Power distribution along the radius span at two different configurations.

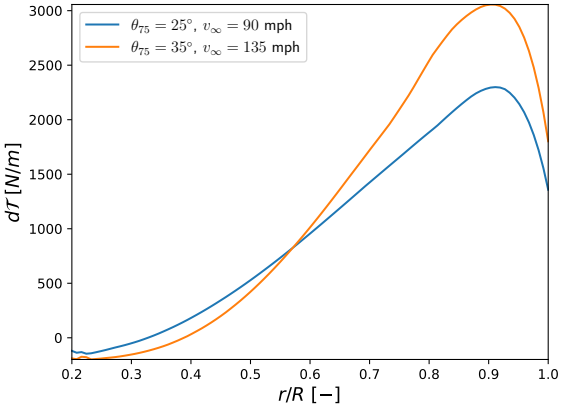

(b) Trust distribution along the radius span at two different configurations.

Figure 3.1: Trust and power distribution the radius span at two different configurations with a rotational speed is 800 RPM..

The analysis can begin by segmenting the curve into several parts. The first segment where the curve is negative, the second segment where it increases linearly to a maximum, and the final segment where it decreases.

- Negative segment: The negative segment occurs because the angle of attack (AOA) is under zero-lift angle of attack. Resulting in a negative $C_{\mathcal{L}}$, which creates negative torque and thrust.
- Linear increase: The relationship appears almost linear because as one moves towards a higher r/R ratio, the blade rotational velocity increases, as shown by $u = \Omega r$. This leads to a different speed triangle which can be shown at the Figure 3.2 with an increasing β, which forms a greater angle of attack, thus increasing $C_{\mathcal{L}}$. Since $C_{\mathcal{L}}$ typically follows a linear curve, the increase is nearly linear.
- Decrease in thrust and power: This reduction is attributed to the tapering of the blades as shown in Figure 1.1, which results in a peak followed by a decline.

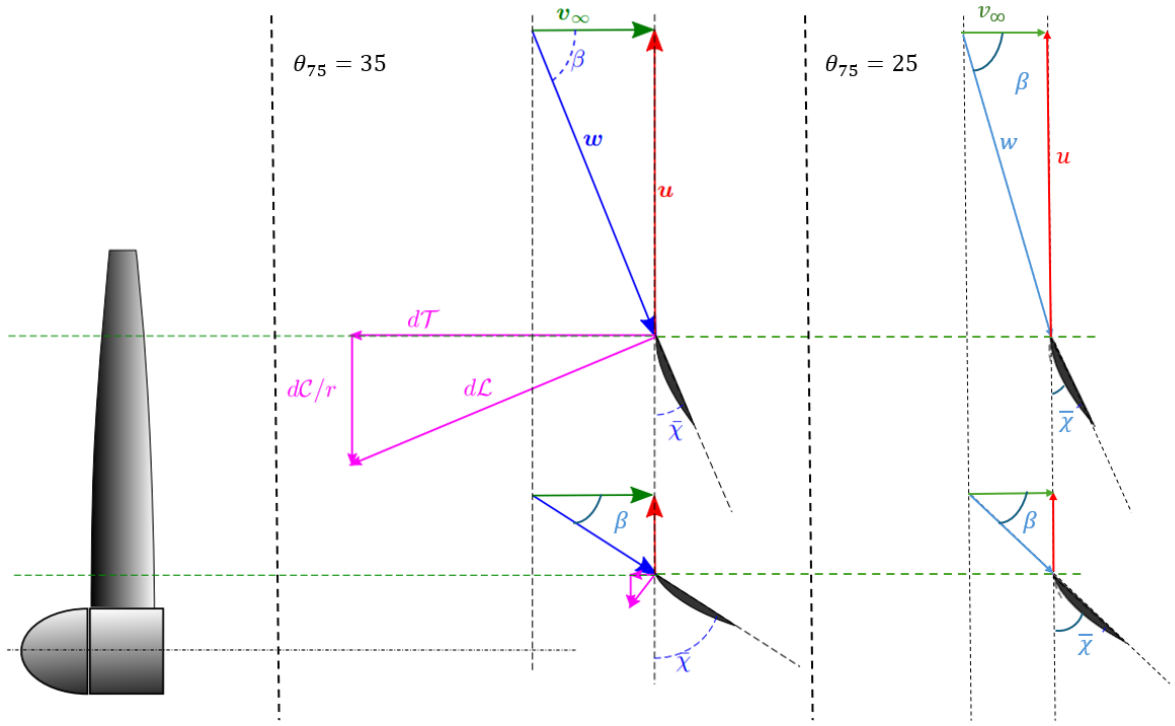

Figure 3.2: Velocity triangles at two different radii, with absolute velocity approximated by the freestream velocity v_∞, relative velocity w and local blade speed u. The local lift force $d\mathcal{L}$ and the corresponding contributions to thrust $d\mathcal{L}_a = d\mathcal{T}$ and torque $dL_u = dC/r$ (purple) drawn to scale, assuming the same chord on both positions. This relation is made for two several θ_{75} configuration

To better understand the differences between the two curves, it is essential to comprehend the impact of θ_{75} on thrust and power.

When θ_{75} is low, which is going to lead to low collective pitch. this configuration is optimal for small wind speed, like the take-off, this can be explained by the fact that the rotational speed u dominates over the wind speed v_∞. Consequently, the angle β, inherently negative, becomes even more negative. This orientation ensures that the lift force is primarily axial (e_a), which increases thrust due to an increase in $d\mathcal{F}_{a,n}$ and reduces torque due to a decrease in $d\mathcal{F}_{u,n}$. This increasing of trust going to lead to a lower propulsion efficiency. If the wind speed increases, β will also increase, leading to a reduction in efficiency. Similarly, if the RPM is reduced, the local blade speed u will decrease, resulting in an increase in β. Conversely, when θ_{75} is high, the optimal point is reached at a higher advance ratio because the axial velocity is relatively high (v_{a2}). In this situation, β will be greater, causing the lift force to deviate from the axial direction, resulting in lower thrust at high flight speeds and higher couple, this lower trust going to lead to higher propulsive efficiency. For further clarification, a diagram illustrating the impact of θ_{75} for both configuration is shown in Figure 3.2. It is important to note that this figure is an approximation because the absolute flow angle was not taken into account for simplification purposes. To better understand the impact of β, refer to Figure 3.3, where you can directly observe the effects of increasing or decreasing β.

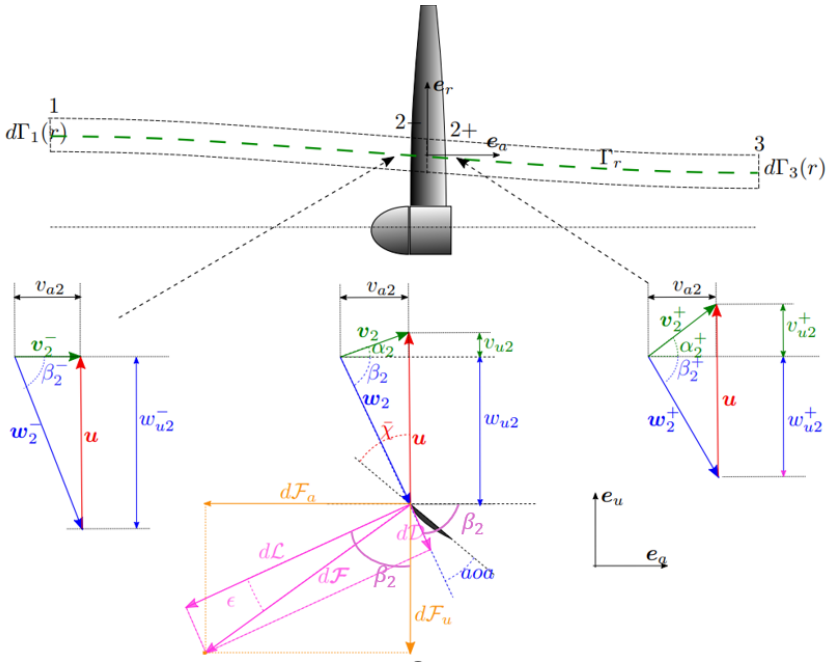

Figure 3.3: The flow triangles just upstream (2^-), at (2) and downstream (2^+) of the propeller, indicating the contribution of the section $[r - dr/2, r + dr/2]$ to the lift $d\mathcal{L}$, drag $d\mathcal{D}$ the force on the propeller dF (taken of the course

4 Comparison of Theoretical and Experimental Propeller Performance

This section discusses the comparison between experimental results [1] and theoretical models, focusing on the performance of the propeller in relation to the advance ratio for $\theta_{75} = 15°$ to $45°$. For a high advance ratio, the RPM will be changed Table 4.1. For increased accuracy, the software WebPlotDigitizer [3] is utilized. This software enables direct extraction of data points from the figures presented in [1], allowing a better comparison of the two curve.

Blade angle [deg]	*Rotational speeds [RPM]*
15	1000
20	1000
25	800
30	800
35	800
40	700
45	700

Table 4.1: Propeller rotational speeds for tunnel speeds below 115 mph. [1]

4.1 Trust coefficient with respect to the advance ratio

The decrease in thrust is due to the effect of the advancing ratio, which is influenced by an increase in β. As β increases and becomes more positive, the flow becomes less aligned, resulting in a continuous reduction in thrust until it eventually reaches zero. [1]
The **??** illustrates the impact of the collective pitch on the thrust coefficient ($C_{\mathcal{T}}$) for different advance ratios ($\mathcal{J}$). Increasing the collective pitch improves the axial input speed (v_{a3}), inducing a phase shift which allows higher $C_{\mathcal{T}}$ to be maintained at increased $\mathcal{J}$. The emergence of bubble shapes at higher settings of θ_{75} signals the onset of stall conditions, which restrict operational efficiency at lower feed rates. For this reason, during the low-speed phase, a lower θ_{75} is favored to enable the propeller to rotate faster without stalling, thus generating more thrust. This graph depicts the beginning of the curve; however, it is capable of extending much further, which would result in increased thrust at a smaller advance ratio. Nevertheless, this extension would also lead to significant power loss and consequently lower efficiency.

[1] The increase in β might seem counterintuitive, but this is because it was initially defined as negative.

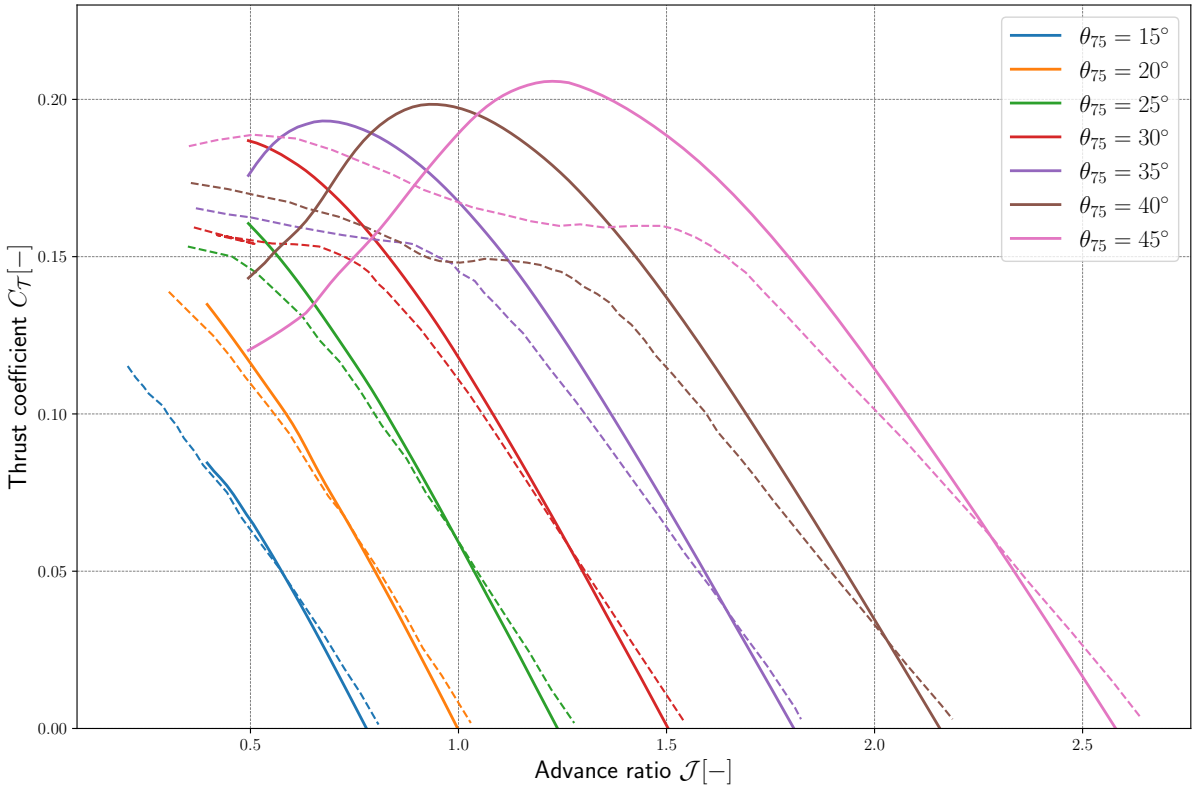

Figure 4.1: Trust coefficient $d\mathcal{T}$ with respect to the advance ratio with θ_{75} ranging from 15-40°

When comparing the data, we observe that the error increases with the collective pitch. This is because a higher collective pitch corresponds to a higher advance ratio, at which the imperfection material become more pronounced, thus contributing to the larger observed error. Additionally, it appears that stall occurs earlier than predicted. This can be attributed to the theoretical analysis, which uses the Rotare software [2]to find the C_L. This software utilizes Xfoil, which cannot precisely estimate the stall. After the stall, the analysis becomes too chaotic to be of interest.

4.2 Power coefficient with respect to the advance ratio

The same phase shift observed with thrust can also be identified in the power coefficient, which is attributable to their mutual dependence on v_{a3}. This is demonstrated in Figure 4.2. The quadratic shape of the curve is due to the power being defined as the product of mass flow rate and enthalpy power. Therefore, it is expressed as a function of v_a^2. It is more complicated to detect the stall due to the quadratic line produced by the power coefficient.

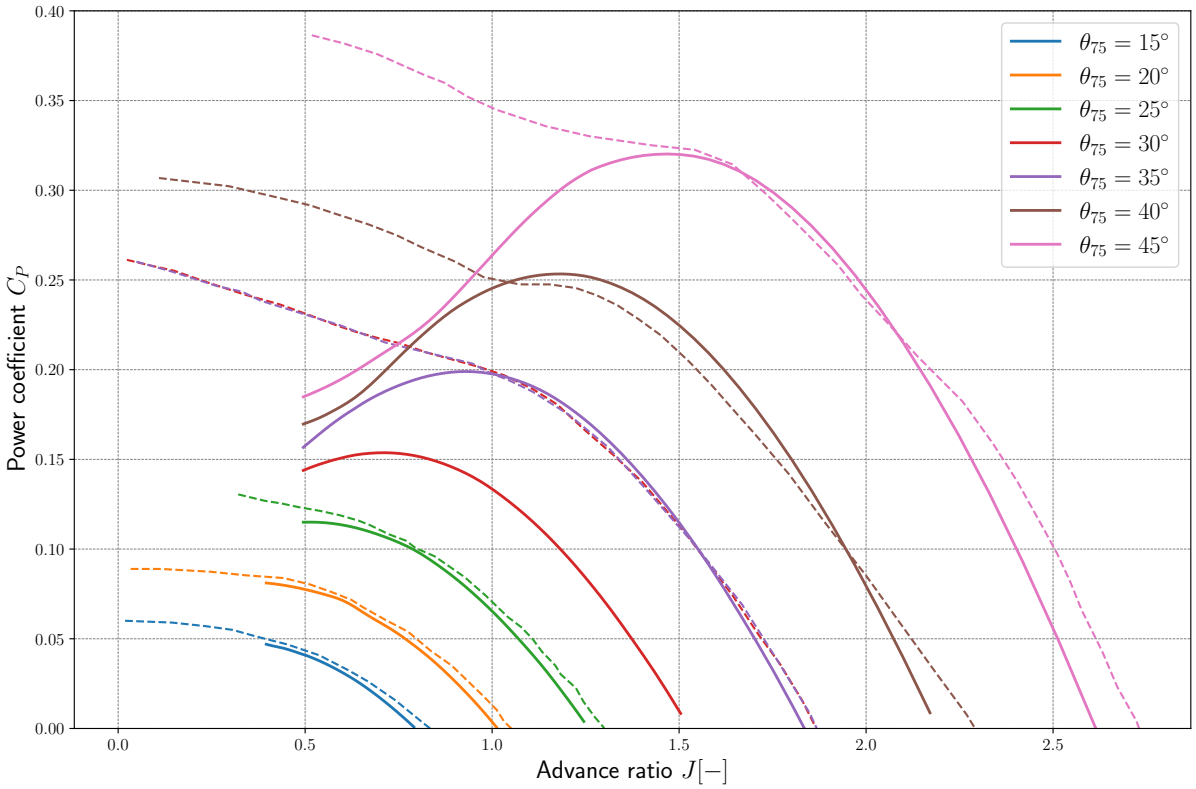

Figure 4.2: Power coefficient $d\mathcal{P}$ with respect to the advance ratio with θ_{75} ranging from 15-40°

The less pronounced error at the beginning can be attributed to the fact that we can trace a line of constant thrust for diverse power settings, as shown in the experimental data [1]. This leads to a smaller error at the beginning of the shape.

4.3 Efficiency coefficient with respect to the advance ratio

Efficiency, defined as the ratio of thrust ($\mathcal{T}$) to power ($\mathcal{P}$) multiplied by the free-stream velocity (v_∞), exhibits distinct behavior with variations in the pitch angle θ_{75} like observed in Figure 4.3. The peak efficiency shifts to higher advance ratios as the collective pitch increases. However, the peak efficiency is lower at smaller pitch angles due to higher thrust, which results in reduced propulsive efficiency. Under normal conditions, the onset of stall would typically cause a sharp decline in efficiency to zero. However, this behavior is not reflected here because stall effects were excluded from consideration, as the blade element momentum theory does not account for them. Furthermore, when the flow is less aligned with the blade, higher hydrodynamic losses occur.

A comparison of the experimental data with the theoretical value reveals that the peak of efficiency is lower than the predicted value. This discrepancy can be attributed to the stall, which occurs at a higher thrust, as illustrated in Figure 4.1.

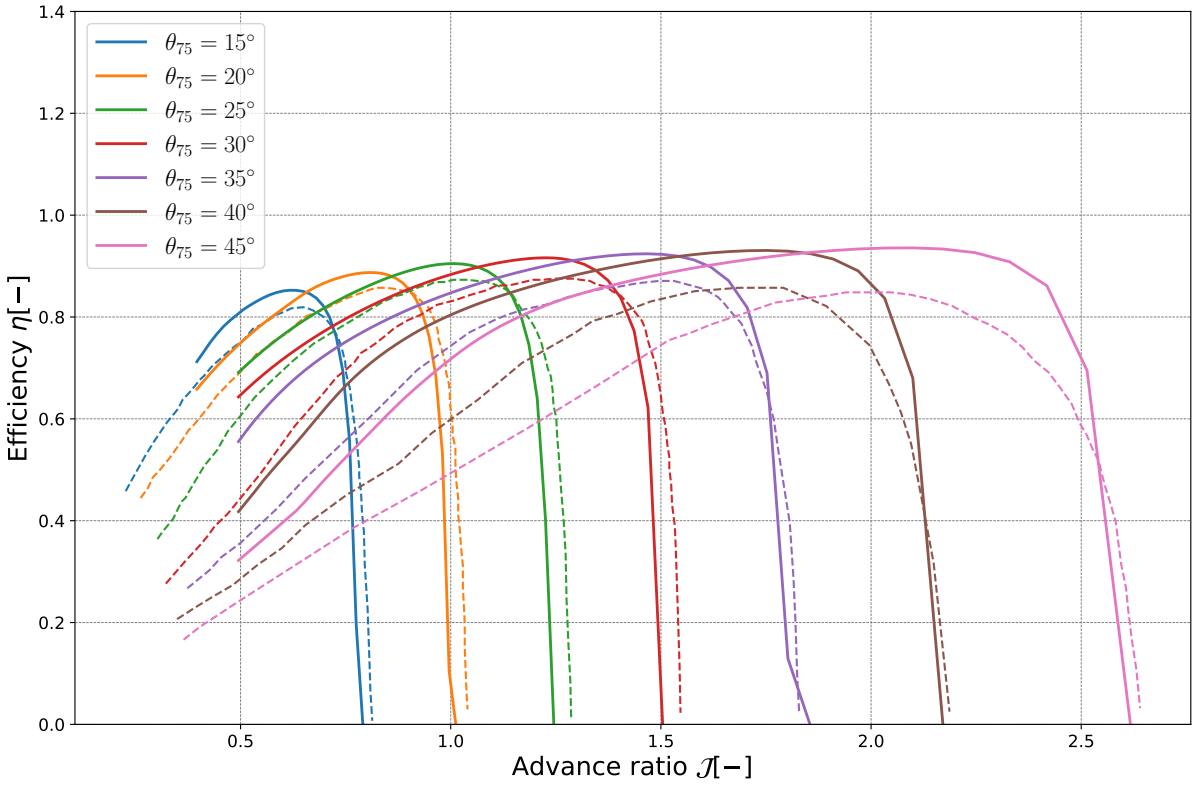

Figure 4.3: Propulsive efficiency η with respect to the advance ratio with θ_{75} ranging from 15-40°

The error here is the combined error of $C_{\mathcal{T}}$ and $C_{\mathcal{P}}$; therefore, it is not particularly interesting to analyze.

5 Conclusion

The aim of this study was to improve understanding of the impact of pitch angle at three quarters span on the 5868-9 three-bladed propeller with a Clark Y profile. The study included a polynomial analysis of lift and drag coefficients as a function of angle of attack, which provided a better understanding of the effects of Reynolds number on these coefficients and improved the understanding of flow separation as a function of angle of attack and Reynolds number.

Furthermore, the investigation extended to an analysis of thrust and power distribution along the span for two different configurations at varying θ_{75} angles. This approach facilitated a more comprehensive understanding of the pitchwise distribution of velocity triangles and the effects that θ_{75} exerts on propeller performance.

In addition, a comparison between theoretical and experimental values was performed to evaluate the propeller's performance across a range of advance ratios, specifically for θ_{75} angles ranging from 15° to 45°. This comparative analysis not only provided a broader perspective on the impact of θ_{75} on performance coefficients but also highlighted the inherent limitations of Blade Element Momentum Theory (BEMT). Specifically, it revealed the significant errors BEMT produces at high advance ratios and its inability to accurately capture the start of stall phenomena. These findings underscore the necessity of considering these limitations in future propeller design and analysis.

A Convergence by Number of Elements per Blade

The convergence of the number of elements per blade is analyzed to assess the cumulative relative error for $d_{\mathcal{P}}$ and $d_{\mathcal{T}}$ as a function of the number of elements, as depicted in Figure A.1.

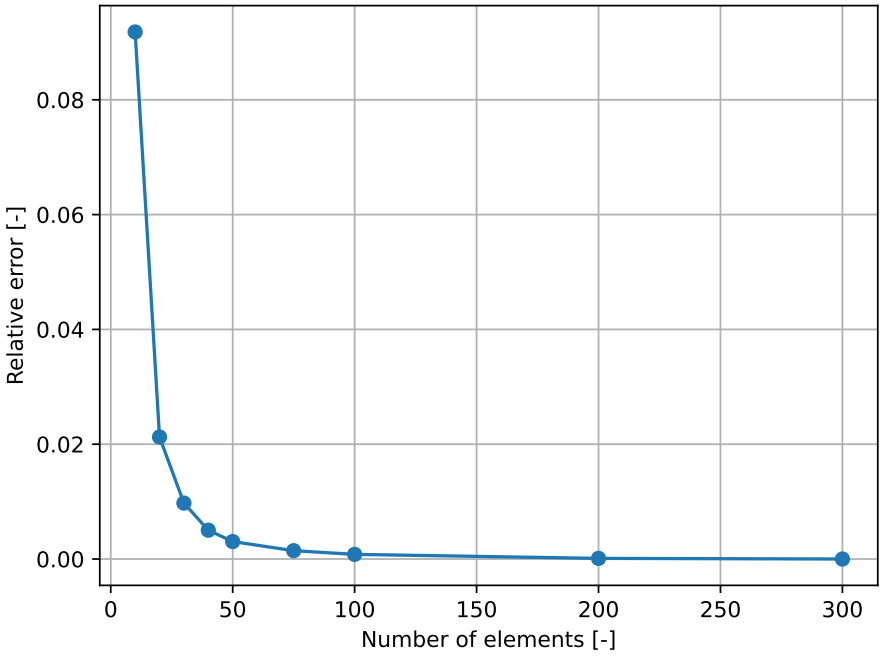

Figure A.1: Convergence of the relative error as a function of the number of elements per blade.

Convergence is observed with 100 elements per blade.

References

[1] David Biermann and Edwin P. Hartman. *The Aerodynamic Characteristics of Six Full-Scale Propellers Having Different Airfoil Sections*. Technical Report NACA-TR-650. Document ID: 19930091725. Available at NASA Technical Reports Server (NTRS). National Advisory Committee for Aeronautics (NACA), 1939. URL: https://ntrs.nasa.gov/search.jsp?R=19930091725.

[2] Thomas Lambert. *ROTARE: A Feature-Rich and Open-Source Implementation of the BEMT in Matlab*. https://gitlab.uliege.be/rotare/documentation. Version 2023.

[3] Ankit Rohatgi. *WebPlotDigitizer*. Version 4.7. 2024. URL: https://automeris.io/WebPlotDigitizer.html.